# Investigation of a turbulent convective buoyant flow of sodium over a backward-facing step

Tobias Schumm ·
Bettina Frohnapfel ·
Luca Marocco

**Abstract** The influence of buoyancy-aided mixed convection on the heat transfer downstream of a sudden expansion of a plane channel is investigated by means of the steady-state Reynolds averaged Navier Stokes (RANS) simulation. A linear eddy viscosity model is used to compute the Reynolds stresses. The turbulent heat fluxes are modelled with a single gradient diffusion hypotheses using a local correlation to evaluate the turbulent Prandtl number. The velocity, turbulent kinetic energy and Reynolds shear stress profiles predicted are in good agreement with available DNS data. The local Stanton number trend is qualitatively well captured, however, its magnitude is underestimated for the mixed convection cases. Compared to the case of forced convection, the flow field and heat transfer change significantly. An influence of buoyancy is reported at very low Richardson numbers (Ri). A steady increase in heat transfer with rising influence of buoyancy is observed.

**Keywords** backward-facing step · mixed convection · liquid metal · RANS models

Tobias Schumm · Bettina Frohnapfel
Institute of Fluid Mechanics, Karlsruhe Institute of Technology, Kaiserstr. 10, Geb. 10.23
Tel.: +49-721-608-42368
Fax: +49-721-608-45147
E-mail: tobias.schumm@kit.edu,
E-mail: bettina.frohnapfel@kit.edu

Luca Marocco
Politecnico di Milano, Department of Energy, via Lambruschini 4, 20156 Milan, Italy

Karlsruhe Institute of Technology (KIT), Institute for Nuclear and Energy Technologies, Hermann-von-Helmholtz-Platz 1, 76344, Eggenstein-Leopoldshafen, Germany
E-mail: luca.marocco@kit.edu

# 1 Introduction

Increased interest in renewable energy sources as well as new and more secure nuclear power plants puts the focus on liquid metals as a heat transfer medium. Due to the fluid properties of liquid metals, especially liquid sodium, the influence of buoyancy on the flow field is present at much higher Reynolds numbers compared to water or gases. The mixed convection flow regime is therefore of great interest for heat transfer applications using liquid metals as a working fluid. As in industrial applications it is most likely to feature changes in cross section or blockages, e.g. spacers between heating rods in nuclear reactors, the knowledge about the influence of a recirculating flow on buoyancy aided mixed convection is of great importance. The most generic and well investigated geometry for such a set-up is the backward facing step. It has been widely studied in literature, both experimentally as well as numerically. Indeed, it is a valuable benchmark to test the capabilities of RANS models in cases with separation and reattachment, which are often found in complex real geometries. For the present study, one recent valuable contribution to the subject has been provided by Klein et al. [1]. They compared several linear and nonlinear eddy-viscosity schemes, Reynolds stress transport models and single- and two-time-scale approaches to experimental data and found out, that the low-Reynolds model of Launder and Sharma [2] returns the best agreement with the measurements. From the heat transfer side less studies are available and all for medium-to-high Prandtl number fluids. This prevents them to be used in the present case with liquid sodium because of the different heat transfer mechanism of liquid metals, as explained in Marocco et al. [3].

Literature about buoyancy-aided mixed convection for liquid metal flows is rare. Buhr et al. [4] showed that mercury (Pr ≈ 0.02) exhibits a decrease in heat transfer with the onset of buoyancy forces, which is attributed to a decrease of the turbulent heat fluxes. For liquid sodium, having an even lower molecular Prandtl number (Pr=0.005-0.01), an increase in heat transfer for a buoyancy-aided mixed convective flow in a vertical pipe has been experimentally and numerically shown by Jackson et al. [5] and Jackson [6].

Recently Niemann and Fröhlich [7,8,9] investigated a turbulent flow of liquid sodium over a backward-facing step at forced and buoyancy-aided mixed convection using direct numerical simulations. Besides a detailed insight on the flow physics, direct numerical simulations also allow to obtain important information for comparison and development of turbulence models. A decrease of the recirculation zone is reported in [8]

---

**Nomenclature**

**Greek Symbols**

| | |
|---|---|
| $\alpha$ | molecular diffusivity |
| $\alpha_t$ | eddy diffusivity of heat |
| $\beta$ | volumetric expansion coefficient |
| $\delta$ | half inlet channel height |
| $\delta_{ij}$ | Kronecker delta |
| $\epsilon$ | dissipation rate of turbulent kinetic energy |
| $\nu$ | kinematic viscosity |
| $\nu_t$ | turbulent eddy viscosity |
| $\rho$ | density |
| $\tau_w$ | wall shear stress |
| $\theta$ | temperature fluctuation |
| $\tilde{\epsilon}$ | homogeneous part of $\epsilon$ |

**Roman Symbols**

| | |
|---|---|
| $\Delta T$ | characteristic temperature difference ($\frac{\dot{q}H}{\lambda}$) |
| $\overline{u_i u_j}$ | time averaged Reynolds stresses |
| $\overline{u_j \theta}$ | time averaged turbulent heat fluxes |
| $c_f$ | skin friction coefficient ($\frac{2\tau_w}{\rho U_b^2}$) |
| $e$ | discretization error |
| $ER$ | Expansion ratio ($\frac{h}{h-H}$) |
| $f$ | elliptic relaxation function |
| $g$ | acceleration due to gravity |
| $Gr$ | Graßhoff number ($\frac{g\beta(T-T_{ref})L^3}{\nu^2}$) |
| $H$ | step height |
| $h$ | channel height after expansion ($2H$) |
| $k$ | turbulent kinetic energy |
| $L$ | an appropriate length scale |

| | |
|---|---|
| $P$ | dynamic pressure |
| $p$ | observed order of the numerical scheme |
| $P_k$ | turbulent kinetic energy production rate |
| $Pe_t$ | turbulent Peclet number ($\frac{\nu_t}{\nu}\mathrm{Pr}$) |
| $Pr$ | molecular Prandtl number |
| $Pr_t$ | turbulent Prandtl number |
| $r$ | refinement ratio |
| $Re_b$ | Reynolds number based on the inlet channel height ($\frac{U_b 2\delta}{\nu}$) |
| $Re_H$ | Reynolds number based on the step height ($\frac{U_b H}{\nu}$) |
| $Ri$ | Richardson number ($\frac{Gr}{Re^2}$) |
| $S$ | strain invariant ($\sqrt{2S_{ij}S_{ij}}$) |
| $S_{ij}$ | rate of strain tensor ($\frac{1}{2}(\frac{\partial U_i}{\partial x_j} + \frac{\partial U_j}{\partial x_i})$) |
| $St$ | Stanton number ($\frac{Nu}{RePr}$) |
| $T$ | static temperature |
| $U$ | streamwise velocity |
| $u$ | velocity fluctuation |
| $u^+$ | friction velocity ($\frac{\sqrt{\tau_w}}{\rho}$) |
| $U_b$ | inlet bulk velocity |
| $U_i$ | velocity component |
| $V$ | wall normal velocity |
| $x_i$ | cartesian grid coordinate |
| $y^+$ | non-dimensional wall distance ($\frac{y}{u^+}$) |

**Subscripts**

| | |
|---|---|
| $ref$ | reference values refer to the inlet temperature |
| $w$ | indicates wall values |

---

for the mixed convection case, compared to the forced convection one. Due to a wall jet, developing above the heater, a decrease of the thermal boundary layer is observed. Schumm et al. [10] studied the influence of different turbulence and heat transfer models on the correct description of the viscous and thermal field for the forced convective turbulent flow of sodium over a backward-facing step. Regarding the skin friction distribution the $k-\epsilon$ models showed the best agreement with the reference data. For the Stanton number distribution, the heat flux correlation of Kays [11] gave the best results, while two equation heat flux models did not show an improved thermal prediction. Based on these findings the influence of heat flux models on the buoyancy-aided mixed convective flow for the same geometry was studied by Schumm et al. [12]. As in the previous study, the heat flux correlation of Kays was compared to a two equation heat flux model. Similar to forced convection, the correlation showed to be superior than the two equation model in terms of the Nusselt number distribution along the heated surface.

The present contribution aims at extending the previous results of [12] on the influence of buoyancy-aided mixed convection on the flow structure and the heat transfer characteristic of liquid sodium at lower and higher Ri numbers by means of steady state RANS simulations. It has been previously found that the Single-Gradient-Diffusion-Hypothesis (SGDH) together with a local correlation for the turbulent Prandtl number proposed by Kays [11] performs well for forced convection and mixed convection to liquid metals in different boundary-layer-like geometries [3, 13,14]. Simulations are performed with different approaches to evaluate the turbulent thermal diffusivity, including the case of $\alpha_t = 0$. The results are compared with DNS data [7].

## 2 Methodology

Within this investigation the incompressible, steady-state Reynolds-averaged Navier-Stokes equations are solved for an incompressible Newtonian fluid with constant thermophysical properties and no viscous dissipation, with the influence of buoyancy accounted for

Table 1: Model functions of the $k - \epsilon$ turbulence model.

| $C_\mu$ | $\sigma_k$ | $\sigma_\epsilon$ | $C_{\epsilon 1}$ | $C_{\epsilon 2}$ | D | E | $f_\epsilon$ | $f_\mu$ |
|---|---|---|---|---|---|---|---|---|
| 0.09 | 1 | 1.3 | 1.44 | 1.92 | $2\nu \left( \frac{\partial \sqrt{k}}{\partial x_i} \right)^2$ | $2\nu\nu_t \left( \frac{\partial^2 U}{\partial x_i \partial x_i} \right)^2$ | $1 - 0.3 \exp\left(-Re_t^2\right)$ | $\exp \frac{-3.4}{(1+Re_t/50)^2}$ |

through the Boussinesq approximation:

$$\frac{\partial U_i}{\partial x_i} = 0 \tag{1}$$

$$U_j \frac{\partial U_i}{\partial x_j} = -\frac{1}{\rho}\frac{\partial P}{\partial x_i} + \frac{\partial}{\partial x_j}\left(\nu \frac{\partial U_i}{\partial x_j} - \overline{u_i u_j}\right) \tag{2}$$
$$+ g_i \beta (T - T_{ref})$$

$$U_j \frac{\partial T}{\partial x_j} = \frac{\partial}{\partial x_j}\left(\alpha \frac{\partial T}{\partial x_j} - \overline{u_j \theta}\right). \tag{3}$$

Unless otherwise specified, in the above equations as well as overall in this paper, Einstein's summation applies to repeated indices. The Reynolds stresses, $\overline{u_i u_j}$, are modelled with Equation (4) and are computed by means of the linear $k - \epsilon$ model of [2], together with the turbulent length scale correction of Yap [15].

$$-\overline{u_i u_j} = 2\nu_t S_{ij} - \frac{2}{3}\delta_{ij}k \tag{4}$$

In previous studies of the present authors [10,12] this model had the best performance for the turbulent flow over a backward-facing step with liquid sodium at forced and buoyancy-aided mixed convection, wherefore it is chosen for this investigation. The eddy viscosity is computed with

$$\nu_t = C_\mu f_\mu \frac{k^2}{\tilde{\epsilon}}. \tag{5}$$

The additional equations solved are:

$$U_j \frac{\partial k}{\partial x_j} = \nu \frac{\partial^2 k}{\partial x_j \partial x_j} + \frac{\partial}{\partial x_j}\left(\frac{\nu_t}{\sigma_k}\frac{\partial k}{\partial x_j}\right) \tag{6}$$
$$+ P_k - \tilde{\epsilon} + D$$

$$U_j \frac{\partial \tilde{\epsilon}}{\partial x_j} = \nu \frac{\partial^2 \tilde{\epsilon}}{\partial x_j \partial x_j} + \frac{\partial}{\partial x_j}\left(\frac{\nu_t}{\sigma_\epsilon}\frac{\partial \tilde{\epsilon}}{\partial x_j}\right) \tag{7}$$
$$+ \frac{\tilde{\epsilon}}{k}\left(C_{\epsilon 1} P_k - C_{\epsilon 2} f_\epsilon \tilde{\epsilon}\right) + E$$

where $\tilde{\epsilon} = \epsilon - 2\nu(\frac{\partial k}{\partial x_j})^2$ is the homogeneous part of the dissipation rate of $k$, and $\sigma_k$ and $\sigma_\epsilon$ are model dependent constants. The production term is defined as

$$P_k = -\overline{u_i u_j}\frac{\partial U_i}{\partial x_j}. \tag{8}$$

The values of the constants $C_{\epsilon 1}$ and $C_{\epsilon 2}$, as well as the damping functions $f_\mu$ and $f_\epsilon$, are reported in Table 1. The turbulent heat fluxes are modelled with the SGDH:

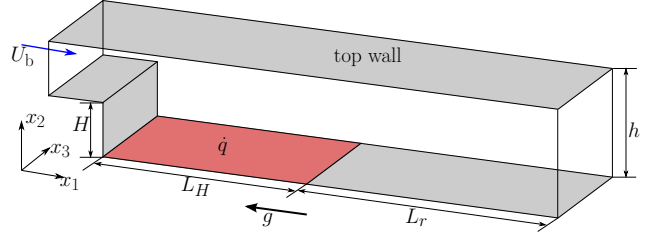$$\overline{u_j \theta} = -\alpha_t \frac{\partial T}{\partial x_j}. \tag{9}$$



Fig. 1: Sketch of the numerical domain.

The turbulent thermal diffusivity is expressed as the ratio between the turbulent viscosity and the turbulent Prandtl number

$$\alpha_t = \frac{\nu_t}{Pr_t}. \tag{10}$$

Instead of using a constant value, $Pr_t$ is computed with the local correlation proposed by Kays [11]:

$$Pr_t = 0.85 + \frac{0.7}{Pe_t}. \tag{11}$$

This correlation is a good fit to DNS simulations performed for turbulent flows in ducts and in external boundary layers for fluids with $0.025 \leq Pr \leq 0.1$ [11].

## 3 Computational set-up

Two-dimensional steady-state RANS simulations were performed using the finite volume code OpenFOAM. The SIMPLE algorithm for the pressure-velocity coupling and a blended scheme between first and second order for the spatial discretization were used.

The computational domain is sketched in Figure 1 with the geometrical dimensions given in Table 2. For all simulations a hydrodynamic fully developed channel flow profile at $Re_b = 10000$ is applied at the inlet, $4H$ upstream of the separation point, while at the outlet a zero-flux boundary condition is set for all variables. At the walls the no-slip condition has been enforced.

Table 2: Geometrical parameters of the simulation.

| H | ER | $L_H$ | $L_r$ |
|---|---|---|---|
| 1 | 2 | 20H | 20H |

Table 3: Overview over the different cases considered at $Re_H = 10000$ and $Pr = 0.0088$.

| Case | 1 | 2 | 3 | 4 | 5 | 6 |
|------|---|------|------|-----|-----|---|
| Ri | 0 | 0.01 | 0.12 | 0.2 | 0.4 | 1 |

Table 4: Calculation of the discretization error for the local skin friction and Stanton number based on the second grid level (medium grid).

| case | $c_f$ | | |
|------|------|----------|-------------|
| | p | $e_{12}$ [%] | $GCI_{12}$ [%] |
| Ri = 0 | 1.09 | 1.09 | 1.34 |
| Ri = 0.12 | 1.77 | 0.43 | 0.44 |
| Ri = 0.2 | 1.98 | 0.29 | 0.35 |
| Ri = 0.4 | 1.71 | 0.41 | 0.50 |
| Ri = 1 | 1.72 | 0.44 | 0.55 |
| | $St$ | | |
| Ri = 0 | 1.84 | 0.16 | 0.2 |
| Ri = 0.12 | 1.60 | 0.20 | 0.25 |
| Ri = 0.2 | 1.99 | 0.09 | 0.12 |
| Ri = 0.4 | 1.67 | 0.07 | 0.09 |
| Ri = 1 | 1.64 | 0.05 | 0.06 |

At the indented wall a constant heat flux has been applied for a length $L_h$ as sketched in Figure 1. All other walls are adiabatic. For forced convection Ri = 0 applies and has been successively increased to investigate mixed convection (see table 3). At all solid walls, $k$ and $\tilde{\epsilon}$ have been set to zero. The adiabatic wall opposite the heater is referred to as "top wall" in the later discussion.

In order to check the numerical error, the Grid Convergence Index (GCI) method of Reder [16], based on Roache [17], was performed for the local skin friction and the local Stanton number distribution above the heater, as both are characteristic variables for this geometry and typically used to describe the model's performance. For the GCI method, a refinement ratio between two successively refined grids of $r = 1.5$ has been used. While the discretization error is expressed by $e$, the GCI is an estimation of an error band, which contains the correct value with a certainty of 95%. The wall averaged streamwise values of $c_f$ and $St$ are given in Table 4. The error based on the finest grid is less than 0.2% for the average Stanton number and less than 1.5% for the average skin friction, thus the grid independency is confirmed. The grids used for this investigation are described in Figure 2 and Tables 5 and 6. The cells are clustered towards the walls, as well as in streamwise direction towards the end of the heater, where steep changes in the velocity gradients are expected. A converged solution is assumed when all of the following conditions are satisfied: (i) constant aver-
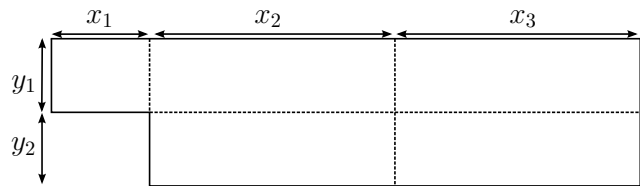


Fig. 2: Schematic sketch of the investigated geometry. The heater is placed directly downstream of the step at the indented wall as indicated in Figure 1.

Table 5: Distribution of the cells for the different meshes used.

| | coarse | middle | fine |
|------|--------|--------|------|
| $N_{y_1}$ | 100 | 150 | 225 |
| $N_{y_2}$ | 100 | 150 | 225 |
| $N_{x_1}$ | 56 | 84 | 126 |
| $N_{x_2}$ | 400 | 600 | 900 |
| $N_{x_3}$ | 150 | 225 | 338 |

Table 6: $y^+$ values at the heater for finest grids used.

| case | $y^+_{min}$ | $y^+_{max}$ | $y^+_{avg}$ |
|------|---------|---------|---------|
| Ri = 0 | 2.5e-3 | 5.6e-1 | 3.3e-1 |
| Ri = 0.12 | 7.6e-4 | 7.7e-2 | 5.8e-2 |
| Ri = 0.2 | 1.2e-3 | 0.9e-1 | 7.1e-2 |
| Ri = 0.4 | 1.9e-3 | 1.1e-1 | 9.1e-2 |
| Ri = 1 | 3.5e-3 | 1.4e-1 | 1.2e-2 |

age skin friction coefficient on the walls; (ii) constant average temperature on the heater; (iii) scaled residuals of all variables is below $10^{-5}$. The results shown in the following discussion refer to the ones of the finest grid available.

## 4 Results

### 4.1 Flow description

The forced convective, turbulent flow over a backward-facing step geometry is characterised by two eddies downstream of the separation point. A small counter-clockwise rotating one in the corner and a clockwise rotating eddy with a large streamwise extent, as shown in the upper picture of Figure 3. The position at which the flow attaches at the lower wall and a boundary layer starts developing is called reattachment point. With increased heating, buoyancy effects start to play an important role. The buoyancy force acts in streamwise direction, thus accelerating the near wall fluid. Consequently, the corner eddy increases in streamwise direction and lifts the recirculation bubble away from the
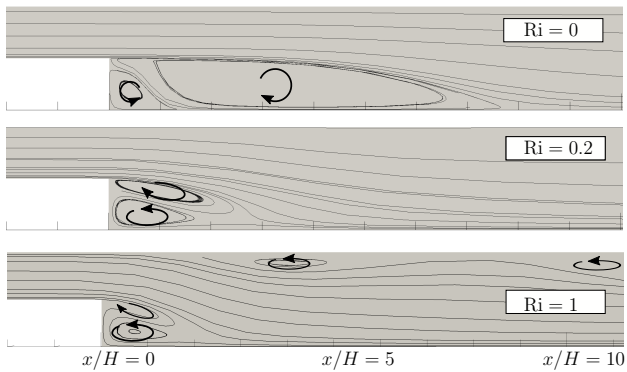
Fig. 3: Streamlines for a turbulent flow over a backward-facing step with forced convection (Ri = 0) and buoyancy-aided turbulent mixed convection (Ri = 0.2), taken from [12].

heated wall, as shown in the middle and bottom pictures of Figure 3.

## 4.2 Comparison with reference data - forced convection

Before further investigating the influence of buoyancy on the flow structure, the forced convective flow over a backward-facing step is considered. Figure 4 shows the skin friction distribution at the heated wall, downstream of the separation point. The turbulence model is capable to predict the important flow structures, namely the recirculation zone and the corner eddy. Further, the skin friction of the developing boundary layer is in accordance with the reference DNS data [7]. The velocity profiles at five positions downstream of the separation point are plotted in Figure 4. The dashed line shows the separating streamline, grey lines represent the contours of zero streamwise velocity. The velocity profiles predicted are in good agreement with the DNS data, apart from the position directly downstream of the step at $x/H = 1$. The incoming fluid "feels" the step at a later position in the RANS simulations than in the DNS. This effect can be better recognized in the profiles of the turbulent kinetic energy and the shear stresses, plotted in Figures 5 and 6. Further downstream, when the shear layer builds up, the profiles of both $k$ and $\overline{u_1 u_2}$ are in good agreement with the reference data. The good agreement between the RANS simulations and the DNS data found for the momentum field, however, is not found to the same extent for the thermal field. The Stanton number is increased compared to the DNS data, as Figure 7 indicates. The finding is not expected, since the model showed good
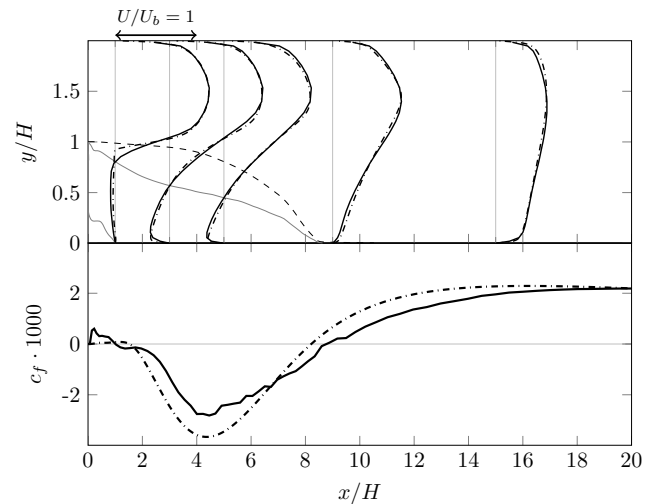


Fig. 4: Upper part: Comparison of the streamwise velocity profiles at different positions downstream of the separation point for Ri = 0. ——: contours of $U = 0$, - - -: separating streamline between the main flow and the recirculation zone, ——: DNS data of [7], -·-·-: RANS data. Lower part: Skin friction distribution downstream of a backward-facing step for Ri = 0. The skin friction distribution is based on private communication with the authors of [7].
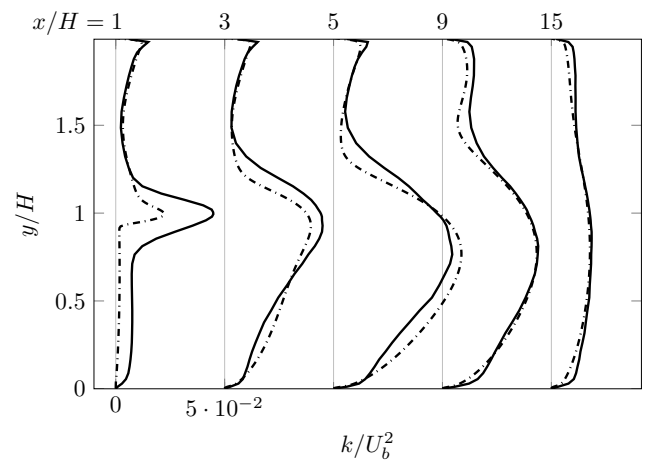


Fig. 5: Comparison of the $k$ profiles at different positions downstream of the separation point for Ri = 0. —— DNS data of [9], -·-·-: RANS data.

agreement for the Stanton number distribution for a turbulent flow over a backward-facing step, however at a different step height, namely $ER = 1.5$ [10]. The overestimation originates from the high turbulent heat flux directly downstream of the separation point, as already shown in Figure 8. The shortcoming of the Kays correlation for the region directly behind the step is based on its dependency on the ratio of eddy to kinematic
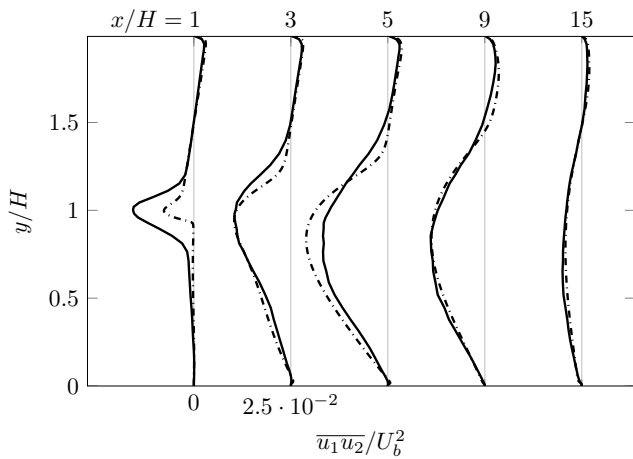
Fig. 6: Comparison of the $\overline{u_1 u_2}$ profiles at different positions downstream of the separation point for Ri = 0. ——: DNS data (private communication based on [9]), -·-·-: RANS data
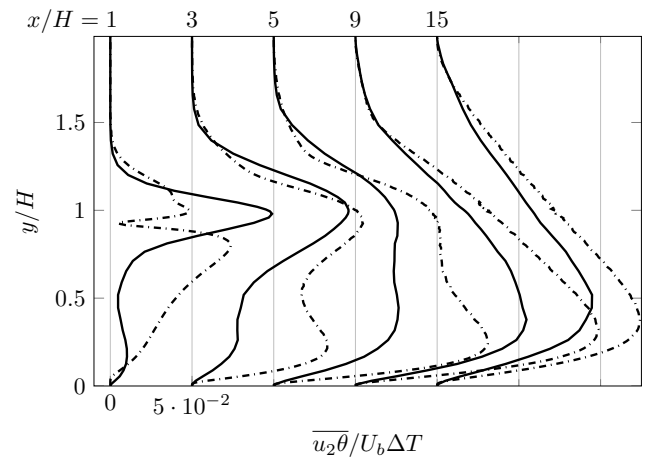


Fig. 8: Comparison of the $\overline{u_2 \theta}$ profiles at different positions downstream of the separation point for Ri = 0. ——: DNS data of [9], -·-·-: RANS data.
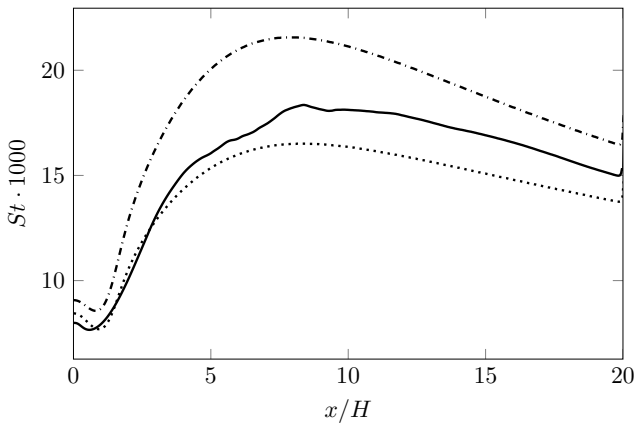


Fig. 7: Comparison of the St profiles at forced convection for Ri = 0. ——: DNS data of [7], -·-·-: RANS data, ·······: RANS data with $\alpha_t = 0$



Fig. 9: Comparison of the ratio of eddy to kinematic viscosity downstream of the separation point for Ri = 0.

viscosity, as shown in Figure 9. Indeed, this correlation has been developed for attached, boundary layer like flows. For $y/H > 1$, the profile of $\nu_t/\nu$ remains almost unchanged and very similar to that of a fully developed channel flow. Already at the position $x/H = 2$, and for $y/H < 1$, the ratio exceeds the typical value of a fully developed channel flow and therefore a larger influence of the turbulent heat fluxes is predicted. As reported in section 2, the Kays correction is based on data for fully developed flows and developing boundary layers, but not for recirculating flows. An additional simulation has been performed with $\alpha_t = 0$ to investigate the importance of the turbulent diffusion of heat on the global heat transfer. The resulting St distribution shows that the molecular diffusion of heat is the dominating energy transport process up to $x/H \approx 4$. Further downstream

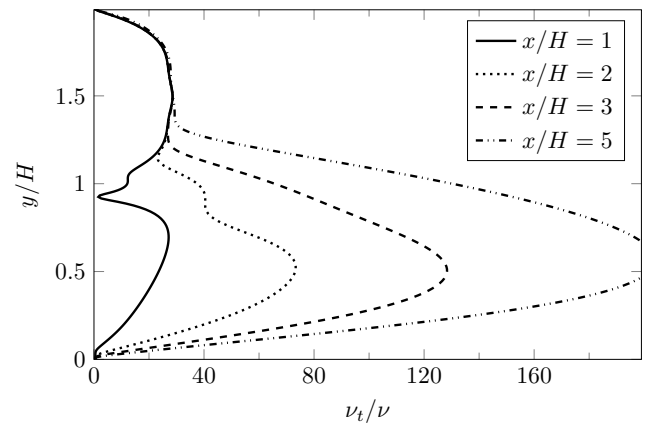the turbulent diffusion of heat has a noticeable contribution to the total heat transport.

4.3 Comparison with reference data - mixed convection

In a first step, the simulations are compared to existing literature data for the cases of Ri = 0.12, 0.2 and Ri = 0.4 [7,9]. Figure 10 shows the $c_f$ distribution at the heater. For all cases a good agreement between the RANS simulations and the DNS data is shown downstream of the separation point. However, the predictions for the case with Ri = 0.2 and 0.4 show a decrease of $c_f$ around $x/H \approx 14$ and $x/H \approx 12$ respectively. This behaviour is caused by the increase in the wall normal turbulent heat transfer, as shown in Figure 11. For the sake of clarity only the data for Ri = 0.12 and 0.2 are
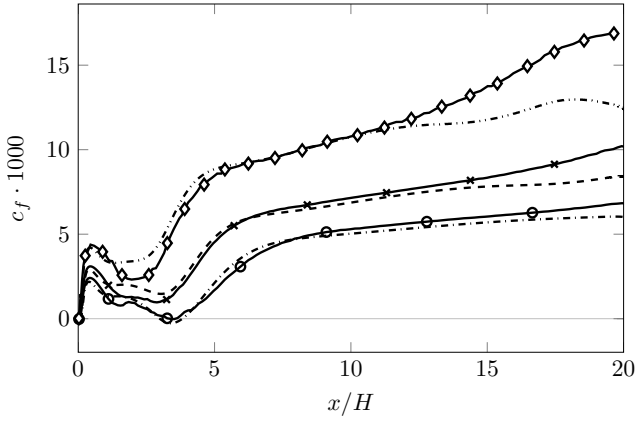
Fig. 10: Comparison of $c_f$ along the side of the heater for different Richardson numbers. DNS data (private comuunication based on [9]): ─⊖─: Ri = 0.12, ─✳─: Ri = 0.2; RANS data: ─·─·─: Ri = 0.12, ─ ─ ─: Ri = 0.2; ─◇─: DNS data based on personal communication with the authors of [9] and ─··─··─: RANS data at Ri = 0.4.



Fig. 11: Comparison of the $\overline{u_2\theta}$ profiles at different positions downstream of the separation point. ─⊖─: DNS data of [7] and ─·─·─: RANS data at Ri = 0.12; ─✳─: DNS data of [9] and ─ ─ ─: RANS data at Ri = 0.2.

shown. But also for Ri = 0.4 the wall normal turbulent heat fluxes are much bigger than those predicted by the DNS. The larger $\overline{u_2\theta}$ profile at $x/H = 15$ leads to a stronger mixing of the fluid temperature. Thus the near wall fluid is cooled down having a positive influence on the heat transfer, indicated by the St profile in Figure 12, and also on $c_f$ due to the reduced near-wall velocity gradients. For all cases the predicted heat transfer is almost overall lower compared to the DNS data of [7], resulting in a higher wall temperature. The SGDH model is not capable to correctly predict the turbulent heat fluxes. One reason lies in its strong simplification, which relates the turbulent heat fluxes to the mean temperature gradients, that does not allow to correctly reproduce the anisotropy eventually present. However, for both cases the discrepancy is less than 10%.

Simulations using the generalised gradient diffusion hypothesis (GGDH) model of Daly and Harlow [18] and Ince and Launder [19], that only accounts for the first term of the general algebraic heat flux model equation (Eq. (12)), did not show an improved heat transfer prediction for the case with Ri = 0.2.

$$\overline{u_j\theta} = -\frac{1}{c_\theta}\frac{k}{\epsilon}\left(\overline{u_iu_j}\frac{\partial T}{\partial x_j} + (1-c_{\theta 2})\overline{u_j\theta}\frac{\partial U_i}{\partial x_j}\right)$$
$$-\frac{1}{c_\theta}\frac{k}{\epsilon}(1-c_{\theta 3})\beta g_i\theta^2 \quad (12)$$

One reason is the use of a linear turbulence model, which provides an inaccurate distribution of the Reynolds stresses, which are included in Eq. 12 and thus very important for more accurate predictions of $\overline{u_j\theta}$. Moreover, ignoring the second term, which accounts
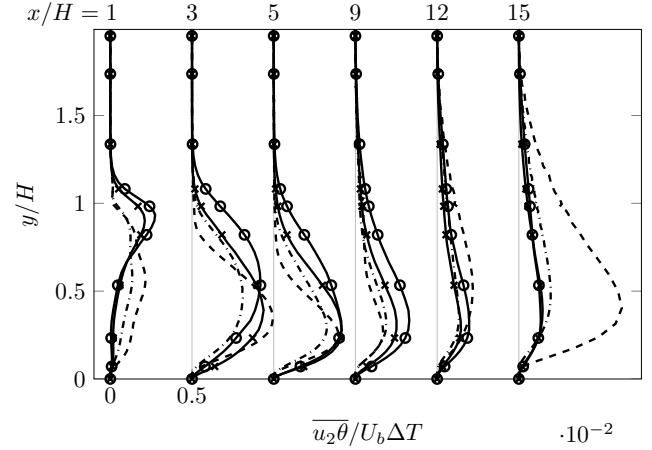


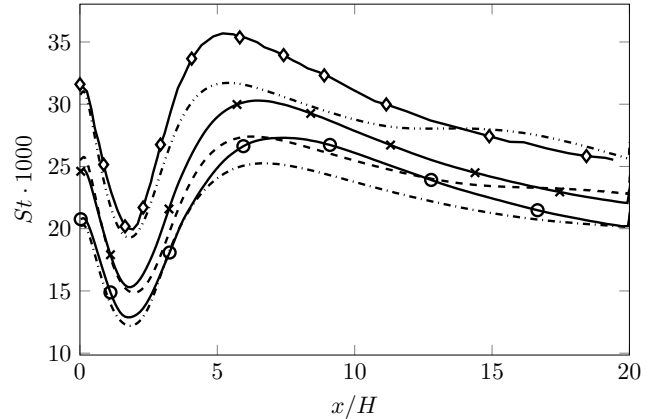Fig. 12: Comparison of $St$ along the side of the heater for different Richardson numbers. DNS data of [7]: ─⊖─: Ri = 0.12, ─✳─: Ri = 0.2; RANS data: ─·─·─: Ri = 0.12, ─ ─ ─: Ri = 0.2; ─◇─: DNS data based on personal communication with the authors of [9] and ─··─··─: RANS data at Ri = 0.4.

for the velocity gradients, could also lead to inaccurate results for recirculating flows. Tests performed by the author showed, that the third term, i.e. the production of turbulent heat fluxes due to buoyancy, can be neglected in the considered range of parameters. However, the model including the first two terms of Eq.(12) has not yet been validated for liquid metals, wherefore a SGDH model is used for this investigation.
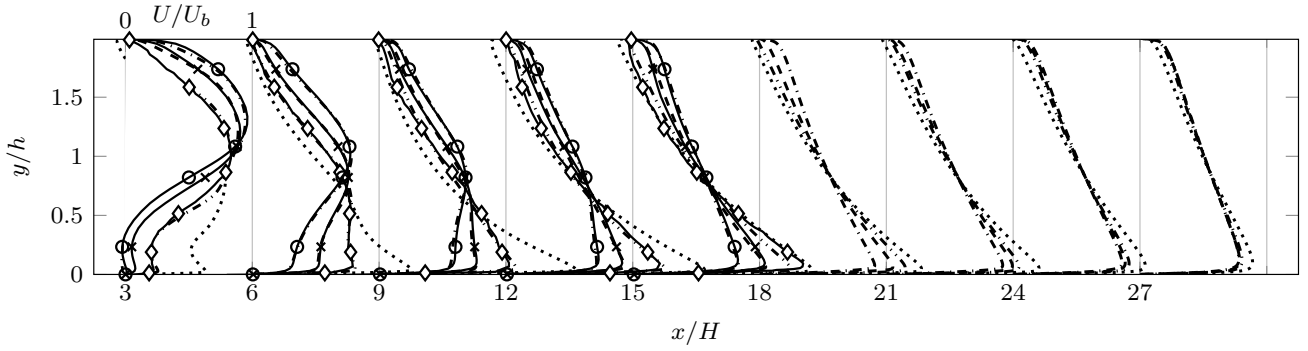
Fig. 13: Comparison to DNS data [9] of the velocity profiles for buoyancy-aided mixed convection. —⊖—: DNS of Ri = 0.12, —×—: DNS of Ri = 0.2, —◇—: DNS of Ri = 0.4 from [9], -·-·-: RANS data for Ri = 0.12, - - -: Ri = 0.2, -··-··: Ri = 0.4, ·······: Ri = 1
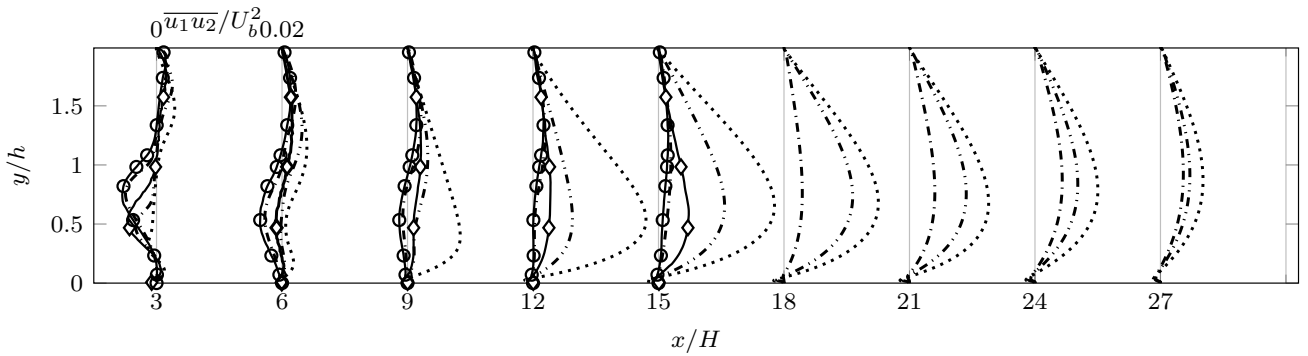


Fig. 15: Comparison to DNS data of the shear stress profiles for buoyancy-aided mixed convection. DNS (private comunnication based on [9]) : —⊖—: Ri = 0.12, —◇—: Ri = 0.4; RANS: -·-·-: Ri = 0.12, -··-··: Ri = 0.4, ·······: Ri = 1

## 4.4 Influence of mixed convection

*Flow field*

The streamwise velocity profiles at several positions downstream of the separation point are shown in Figure 13 for $Ri = 0.12$, 0.2, 0.4 and 1. The simulation at Ri = 1 exceeds the range of available DNS data, such that no comparison can be made. For the first three cases, good agreement with the DNS data is found. As shown in Figure 3 the recirculation zone is reduced in its streamwise extent with increasing buoyancy. Indeed, the velocity profiles get inverted with respect to Ri = 0, with their peak forming above the heater as shown in [12]. Due to continuity, this leads to deceleration of the fluid close to the top wall. For the two cases featuring the highest buoyancy effect, a recirculation at the top wall is indicated by $U < 0$ in Figure 13 and shown in Figure 3 for Ri = 1. While for $Ri = 0.4$ the flow attaches at the top wall at $x/H = 9$ and detaches again further downstream. At $x/H = 12$ the largest peaks in negative and positive streamwise velocity occur for the case with $Ri = 1$. From there on the velocity profiles of the latter case show an increase of the boundary layer
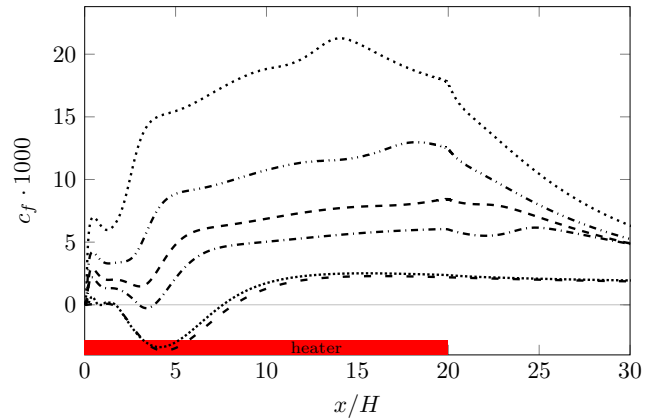


Fig. 14: Influence of buoyancy on $c_f$ along the side of the heater for different Richardson numbers. - - : Ri = 0, ·········: Ri = 0.01, -·-·-: Ri = 0.12, - - -: Ri = 0.2, -··-··: Ri = 0.4, ·······: Ri = 1

thickness on the heated wall, thus reducing the peak in streamwise velocity near the heater as also shown by the reduction of $c_f$ values in Figure 14. Downstream of the heater the flow is slowed down due to the effect of

viscous forces and the absence of the heat source. At the position $x/H = 27$ only minor differences in the velocity profiles are apparent, leading to the conclusion that the cases with higher buoyancy relax faster than those with lower buoyancy influence. This effect is associated with the shear stress distribution shown in Figure 15. Larger shear stresses lead to a higher relaxation rate of the velocity profiles downstream of the heater.

For the turbulent kinetic energy, the differences between the DNS data and the RANS simulations are more pronounced than for the velocity field as shown in Figure 16. Shortening the recirculation zone with increasing influence of buoyancy leads to a reduced $k$ profile downstream of the step, as $k$ is generated in the shear layer originating from the separation point. Close to the heater, the modification of the velocity field by buoyancy leads to small velocity gradients in wall normal direction for $6 \leq x/H \leq 12$ for $Ri \leq 0.4$ as shown in Figure 13 and [12]. Thus, the production of $k$ is suppressed due to the negligible strain rate magnitude. Within this region, a good agreement with the DNS data is apparent. With the developing peak in the velocity profile above the heater further downstream, strong shear stresses are generated causing the production of $k$ around the center of the section ($y/H \approx 0.5$). However, the production is stronger than indicated by the DNS data, especially for $y/H \geq 0.5$.

*Skin friction*
The skin friction distribution along the heater for the different cases is shown in Figure 14. The buoyancy force, acting in streamwise direction, accelerates the fluid close to the heater leading to an increase of $c_f$. Deviations from the $c_f$ profile are already obvious for a small Richardson number such as $Ri = 0.01$. The additional momentum in the fluid amplifies the extension of the corner eddy along the heater, which lifts off the recirculation zone from the heater (for $Ri \geq 0.12$), as reported in [7,8,12]. The reduction of the recirculation zone leads to an upstream shift of $c_{f,min}$ for larger $Ri$. The small region of a decrease in $c_f$ is followed by a steep increase originating from the impinging effect of the inflow. The nearly linear increase of the skin friction following this "impinging" region comes from changes of the velocity profile due to the acceleration of the near wall fluid. The slope of both regions increases with increasing buoyancy. For the cases with $Ri \geq 0.4$, a region with decreasing $c_f$ is apparent towards the end of the heater. This effect originates from different mechanisms. Figure 17 shows for both cases a positive wall normal velocity component transporting momentum away from the heater towards the upper wall, which contributes to a
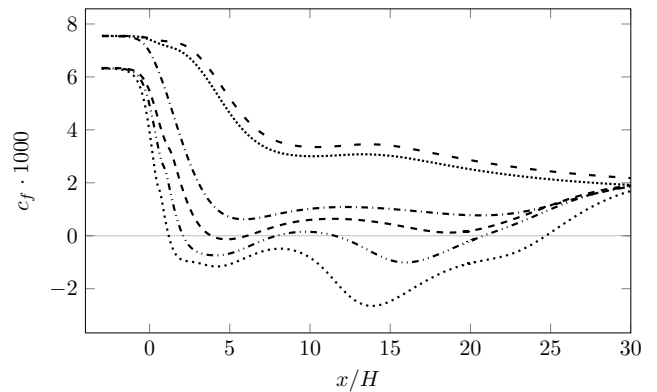


Fig. 19: Comparison of $c_f$ along the adiabatic wall for different Richardson numbers. - - : RANS data for Ri = 0, ⋯⋯: Ri = 0.01, -·-·: Ri = 0.12, - - -: Ri = 0.2, -··-·: Ri = 0.4, ⋯⋯: Ri = 1

better mixing of velocities and decreases the velocity gradient. Furthermore, the high shear stresses lead to a stronger turbulent thermal diffusion hence a better mixing of the thermal field. This leads to a lower wall temperature on the heater and a higher one on the top, as it is apparent in Figure 18. Consequently the buoyancy forces are reduced compared to the positions further upstream, thus reducing $c_f$. Downstream of the heated length the skin friction decreases due to the deceleration of the flow near the indented wall and tends towards the $c_f$ value for $Ri = 0$.

The $c_f$ distribution at the top wall is presented in Figure 19. For the forced convection case, the typical distribution is shown. The skin friction decreases only slightly downstream of the separation point. As soon as the interaction between the inflow and the recirculation zone increases, $c_f$ drops until the reattachment point. From there on, the curve converges slowly towards the same value as on the lower wall. With the onset of buoyancy the fluid is drawn towards the heater, as shown in Figure 3 by the curved streamlines, resulting in a steep decrease of velocity gradients at the top wall. For $Ri = 0.2$ a small recirculation zone appears, indicated by $c_f < 0$. A further increase of buoyancy enlarges the recirculation zone in streamwise direction.

*Stanton number*
In Figure 20 the local St profiles for different Ri are shown. As soon as buoyancy influences the flow structure, all St profiles exhibit a local minimum at the same streamwise position, $\approx 2H$, behind the separation point, followed by a steep increase. Also the case with $Ri = 0.01$ shows this trend directly behind the step, where the highest temperature, thus the strongest buoyancy force, occurs. With increasing
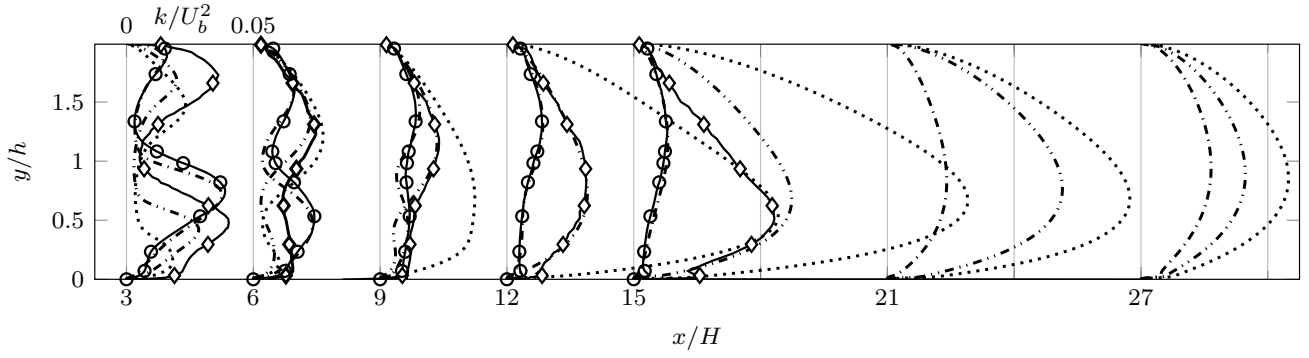
Fig. 16: Comparison to DNS data [9] of the $k$ profiles for buoyancy-aided mixed convection. DNS: —⊖—: Ri = 0.12, —◇—: Ri = 0.4; RANS: —·—·: Ri = 0.12, —··—·: Ri = 0.4, ·······: Ri = 1
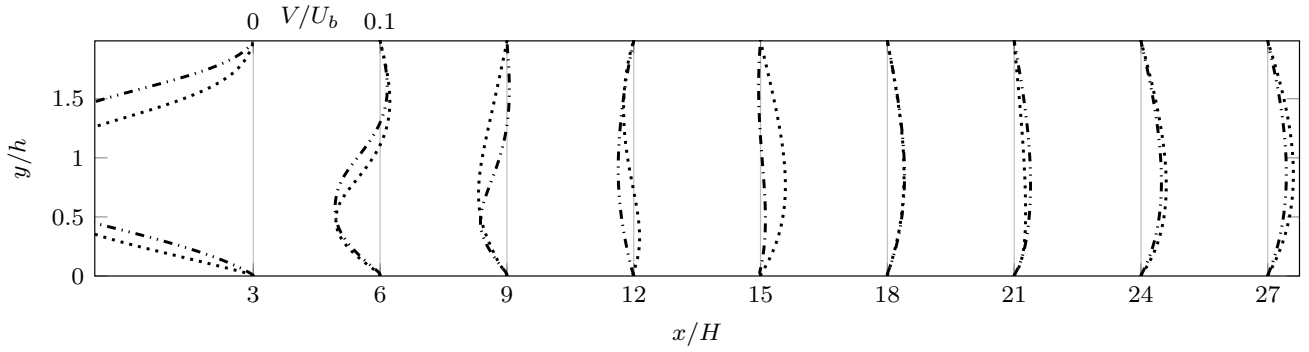


Fig. 17: Comparison of the wall normal velocity profiles for buoyancy-aided mixed convection. —··—·: Ri = 0.4, ·······: Ri = 1
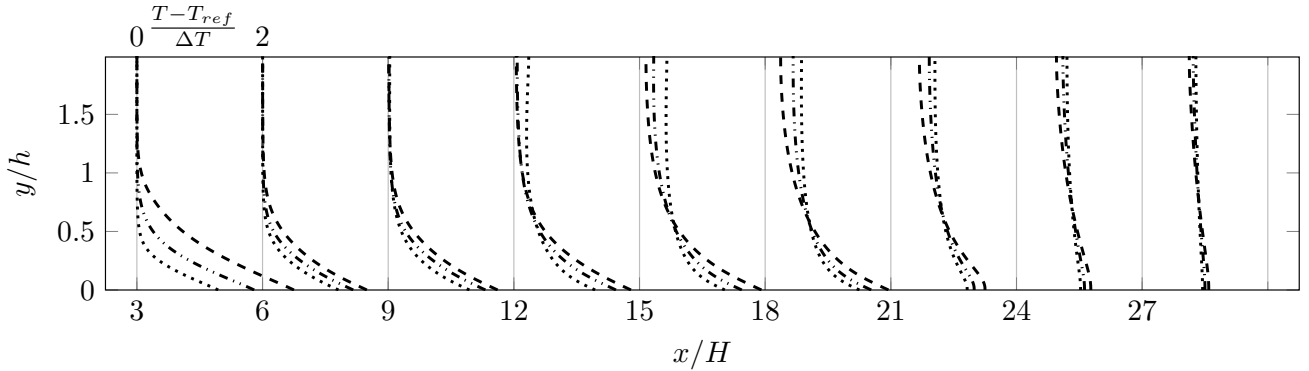


Fig. 18: Comparison of the non dimensionalised temperature profiles for buoyancy-aided mixed convection. — — —: Ri = 0.2, —··—·: Ri = 0.4, ·······: Ri = 1

influence of buoyancy, the heat transfer is enhanced due to the amplified convection, expressed by the increase of the St distribution. Further, the slope of St between $2 \leq x/H \leq 6$ steepens as a result of the impinging like behaviour of the mean flow, shown by the streamlines in Figure 3. By comparing the Stanton number distribution in Figure 20 with that of $c_f$ in Figure 14, it is evident how the Reynolds analogy does not hold for this type of flow and geometry for

mixed convection. Indeed, the transport mechanism influencing $c_f$ is different from that influencing St, as can be deduced from the different trend of the curves, e.g. between $5 \leq x/H \leq 15$ $c_f$ increases, while St decreases.
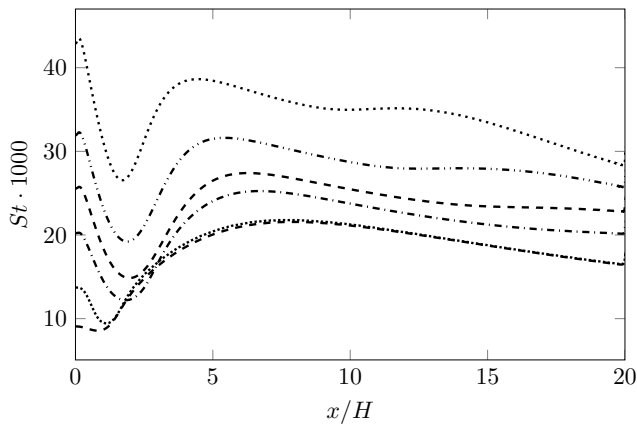
Fig. 20: Comparison of $St$ along the side of the heater for different Richardson numbers. - - : RANS data for Ri = 0, ·········: Ri = 0.01, -·-·-: for Ri = 0.12, - - -: for Ri = 0.2, -··-·: for Ri = 0.4, ······: for Ri = 1

## 5 Conclusion

Within this research the influence of buoyancy-aided mixed convection of liquid sodium on a turbulent flow over a backward-facing step has been investigated by means of two-dimensional steady-state RANS simulation using a linear $k - \epsilon$ model in combination with the local correlation of Kays to account for the eddy diffusion of heat. Buoyancy contributes in accelerating the fluid in vicinity of the heater. Due to continuity, the incoming flow is diverted towards the heated wall more strongly than for the forced convection case. Hence the flow starts separating on the opposite wall of the heater around Ri = 0.2, accentuating with the influence of buoyancy. Furthermore, the inlet flow impinges on the heater earlier with increasing influence of buoyancy leading to a higher heat transfer. Towards the end of the heater, a decrease in $c_f$ is found for the cases with Ri = 0.4 and 1. This decrease is attributed to the strong increase in turbulent shear stresses which counter acts the buoyancy force and decelerates the fluid, thus reducing the near wall velocity gradients. For the region directly behind the step, molecular diffusion of heat is dominant. The influence of eddy diffusion of heat increases further downstream, as the turbulence is generated by the high shear stresses. Nevertheless, the acceleration of near wall velocity is responsible for the enhanced heat transfer found for increasing buoyancy. A similar behaviour is also found in experiments made in a vertical pipe for liquid sodium at a lower molecular Prandtl number of Pr = 0.005 [5,6]. For other liquid metals, i.e. mercury or sodium-potassium, a decreased heat transfer was found for the buoyancy aided mixed convective flow in a vertical pipe at $Pr \approx 0.02$ due to

the larger influence of the turbulent heat flux on the total heat transfer rate. Therefore further investigations on the heat transfer for buoyancy-aided mixed convection flow at higher Prandtl and Reynolds numbers are necessary to estimate the importance of a recirculating flow in applications like solar power plants or nuclear reactors.

## References

1. T. Klein, T. Craft, H. Iacovides, International Journal of Heat and Fluid Flow **51**, 229 (2015)
2. B. Launder, B. Sharma, Letters in Heat and Mass Transfer **1**(2), 131 (1974)
3. L. Marocco, G. Cammi, J. Flesch, T. Wetzel, International Journal of Thermal Sciences **105**, 22 (2016)
4. H.O. Buhr, E.A. Horsten, A.D. Carr, ASME. J. Heat Transfer (1974)
5. J.D. Jackson, B.P. Axcell, A. Walton, Experimental Heat Transfer **7**(1), 71 (1994)
6. J.D. Jackson, in *The 14th International Topical Meeting on Nuclear Reactor Thermal Hydraulics (NURETH-14)* (2011)
7. M. Niemann, J. Fröhlich, in *ERCOFTAC WORKSHOP Direct and Large-Eddy Simulation 10* (2015)
8. M. Niemann, J. Fröhlich, International Journal of Heat and Mass Transfer **101**, 1237 (2016)
9. M. Niemann, J. Fröhlich, in *11th International ERCOFTAC Symposium on Engineering Turbulence Modelling and Measurements* (2016)
10. T. Schumm, M. Niemann, F. Magagnato, L. Marocco, B. Frohnapfel, J. Fröhlich, in *Turbulence, Heat Mass Transfer*, vol. 8, ed. by K. Hanjalic, T. Miyauchi, D. Borello, M. Hadziabdic, P. Venturinie (Begell House, 2015), vol. 8, p. 277280
11. W.M. Kays, Journal of Heat Transfer **116**(2), 284 (1994)
12. T. Schumm, B. Frohnapfel, L. Marocco, Journal of Physics: Conference Series **745**(3) (2016)
13. L. Marocco, A. Alberti di Valmontana, T. Wetzel, International Journal of Heat and Mass Transfer **105**, 479 (2017)
14. Z. Ge, J. Liu, P. Zhao, X. Nie, M. Ye, Nuclear Engineering and Design **314**, 198 (2017)
15. C. Yap, Turbulent heat and momentum transfer in recirculating and impinging flows. Ph.D. Thesis Manchester Univ. (England), Manchester University (England) (1987)
16. M. Reder, In German: Bestimmung des numerischen Fehlers für turbulente Strömungen ber eine zurückspringende Stufe, English translation: Numerical uncertainties in the simulation of a backward-facing step. B.S. Thesis, Karlsruhe Institute for Technology (2016)
17. P.J. Roache, Journal of Fluid Engineering **116**(3) (1994)
18. B.J. Daly, F.H. Harlow, Physics of Fluids **13**(11), 2634 (1970)
19. N. Ince, B. Launder, International Journal of Heat and Fluid Flow **10**(2), 110 (1989)